APL Materials

Flexible, strain gated logic transducer arrays enabled by initializing surface instability on elastic bilayers

Cite as: APL Mater. 7, 031509 (2019); https://doi.org/10.1063/1.5079403
Submitted: 30 October 2018 . Accepted: 13 March 2019 . Published Online: 28 March 2019

Cong Wang, Ben Bin Xu, Jonathan G. Terry, Stewart Smith, Anthony J. Walton, Steven Wang, Haibao Lv, and Yifan Li

Flexible, strain gated logic transducer arrays enabled by initializing surface instability on elastic bilayers

Cite as: APL Mater. 7, 031509 (2019); doi: 10.1063/1.5079403
Submitted: 30 October 2018 • Accepted: 13 March 2019 •
Published Online: 28 March 2019

Cong Wang,[1] Ben Bin Xu,[1,a)] Jonathan G. Terry,[2] Stewart Smith,[2] Anthony J. Walton,[2] Steven Wang,[3] Haibao Lv,[4] and Yifan Li[1,a)]

AFFILIATIONS

[1]Department of Mechanical and Construction Engineering, Faculty of Engineering and Environment, Northumbria University, Newcastle upon Tyne NE1 8ST, United Kingdom
[2]SMC, Institute for Integrated Micro and Nano Systems, School of Engineering, The University of Edinburgh, Edinburgh EH9 3JF, United Kingdom
[3]School of Chemical Engineering and Advanced Materials, Newcastle University, Newcastle upon Tyne NE1 7RU, United Kingdom
[4]Science and Technology on Advanced Composites in Special Environments Laboratory, Harbin Institute of Technology, Harbin 150080, China

[a)]**Authors to whom correspondence should be addressed:** yifan.li@northumbria.ac.uk and ben.xu@northumbria.ac.uk

ABSTRACT

Developing flexible sensors with a high strain sensing range could enable widespread downstream applications, by allowing intimate, mechanically conformable integration with soft biological tissues. By characterizing interconnected metal electrode arrays on super-flexible substrates, we have established a surface deformation control strategy of an array of strain transducers. The strain gated switches are capable of measuring various compressive strains (up to 60%) by bringing metal electrodes into self-contact via creasing elastic instability beyond a threshold substrate strain. The designed devices have been developed to explore the geometry design effect on the electrode-elastomer "stiff film on soft elastomer" surface deformation. The enabled transducer array yielded a stepwise strain-electrical resistance switching mechanism which opens up the potential of future interconnected sensor array type of super-compressible devices.

Flexible electronics and transducers where devices are subject to stretching, bending, and twisting forces have grown into one of the more interesting technologies for next generation applications such as bio-medical electronics, smart skin, wearable sensors, epidermal electronics, and sensors and actuators.[1–10,12,16] Recent research on elastic substrates complying with local features such as metal interconnects and integrated transducers has shown great potential to withstand high strain deformation during bending, compressing, and stretching.[7,12–14] Such structured elastic surfaces under compression and stretching can undergo various deformations such as wrinkling, creasing, folding, and buckling, which generates interest in engineering applications in sensing and actuation.[11,15–25] Among them, recently developed metal-elastomer strain gated transducers have utilized mechanically gated super-flexible electrical switches to provide sensing mechanisms for wearable electronics.[5,8,9,23]

Controllably and reversibly generating creasing and other instability patterns on the surfaces of soft materials by electrical,[26] temperature,[27] mechanical,[28] and electrochemical[29] stimulations have attracted considerable interest in developing them into sensing and actuation applications. One of the latest super-compressible (up to 60%) strain-gated electrical switching sensing mechanisms utilizes surface instabilities such as wrinkles and creases on soft elastomer substrates under compression with stiff film patterns on top (e.g., metal electrodes).[5] Such devices with single-pair of metal "finger" electrodes relying on the controllable formation of surface

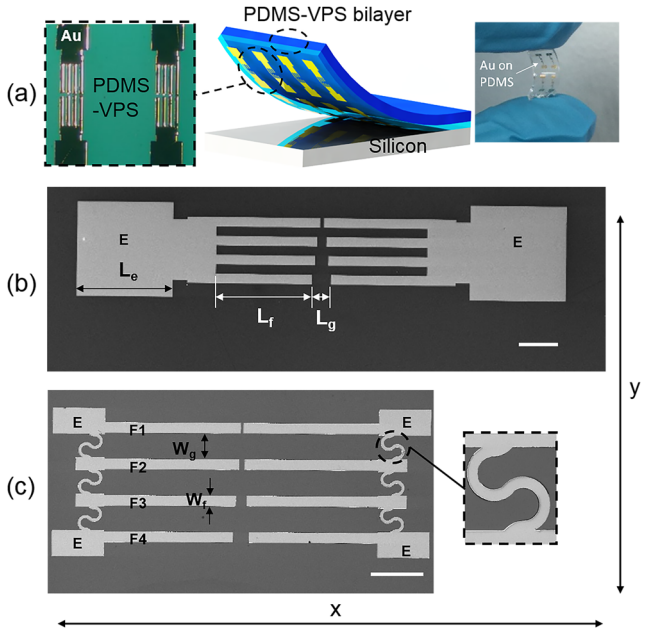

FIG. 1. (a) Schematic (middle) and microscopic image (left) of patterned multi-switching Au strain transducer array, with Au patterns transferred from silicon to the PDMS-VPS substrate by a dual-SAM (self-assembly monolayer) assisted metal transfer process. SEM top-view images showing two different interconnect configurations: (b) 4 pairs of finger transducers "F" interconnected with two bulk contact electrodes "E"; (c) 4 pairs of finger transducers interconnected with contact electrodes by serpentine structures (scale bars = 200 μm).

creases to bring initially disconnected regions of the metal electrode into self-contact were previously reported.[5] When compressed (x-direction in Fig. 1), the stiff Au film (Young's modulus 50–70 GPa) wrinkles due to its near inextensibility. The much softer (Young's modulus 0.4–4 MPa) substrate areas in the gap between Au electrodes can have greater deformation due to the local amplification of strain by the stiff films nearby. At higher compression, a crease forms in this gap between electrodes, generating the desired electrodes' self-contact switching mode.[5] The measured resistance displayed a significant step change from ~10^{13} Ω to ~10^{2} Ω after the self-contact of the electrodes after the substrate compression strain surpasses threshold values.[5] The switching threshold strains can be controlled by geometry design (e.g., Au electrode width W_f, length L_f, and gap width L_g) as well as material and structural properties,[5] and recent research in surface instabilities has shown that the deformation mode can also be controlled via such designs.[21] Moreover, the latest study into surface instabilities on such heterogeneous surfaces with patterned regions of different materials (e.g., stiff metal electrodes and soft elastomers) opens the possibilities for research into advanced surface morphing and more complex application devices.[21]

For future development of transducer arrays applied to a larger area under compression, it is important to develop electrode interconnect technologies which should ultimately enable row-column addressing. This paper discusses a multi-finger switching mechanism with the controllable competing elastic instability growth on super-flexible surfaces, by design and micro-engineering interconnect more complex Au on polydimethylsiloxane-vinylpolysiloxane (PDMS-VPS) bilayer structures. Such a structure was fabricated by a dual-SAM (self-assembly monolayer) assisted metal transfer process which transfers photolithographically patterned Au electrodes (thickness = 74 nm) from silicon to the PDMS-VPS substrates [Fig. 1(a)] with details given in the supplementary material, providing a stepwise resistance-strain response sensing mechanism which could shed light on the future applications in widespread downstream applications, tunable and stretchable electronics.[24–28] This work also experimentally studied instabilities (patterned stiff and soft regions) on heterogeneous surfaces under large compression strains (up to 60%) which could help the development in related theoretical studies, such as that initiated in Ref. 21.

The designed and fabricated transducer arrays and interconnects are shown in Fig. 1. Each of the paired Au finger electrodes based on the previous design[5] with key dimensions (e.g., finger electrode width W_f, length L_f, and gap width L_g) was interconnected by two different configurations. Figure 1(b) shows the SEM image (Tescan® Mira3) of the bulk interconnect configuration linking 4 pairs of finger electrode transducers (labeled F1 to F4) with 2 contact electrodes (labeled E). Figure 1(c) shows the serpentine interconnect configuration which helped protecting the Au electrodes from damage caused by perpendicular direction stretching due to Poisson effect (see details in the supplementary material). This research focuses on the relationship between the geometry design parameters such as W_f, L_f, and L_g and 2D (top-view) deformation for the Au electrodes and gaps in-between at different substrate compression strains ε_{sub}. Other parameters such as the contact electrode length L_e and the adjacent serpentine interconnect spacing W_g [Fig. 1(c)] were also considered.

The uniaxial (x-direction) substrate compression was provided by releasing the pre-stretched PDMS-VPS mounting layer from L_0 to L. Wrinkles on Au finger electrodes started to develop at low strain, and eventually both wrinkles on Au and creases on PDMS after substrate strain $\varepsilon_{sub} = (L_0 - L)/L_0$ went beyond threshold as illustrated in Fig. 2(a). Figures 2(a) and 2(b) show that the reversible wrinkling process on Au has reduced the finger length from L_{f0} to L_f, resulting in a local strain change $\varepsilon_{Au\text{-}x} = (L_{f0} - L_f)/L_{f0}$. Meanwhile as discussed, the gap area in-between (softer PDMS surface) will have its local strain amplified due to surrounding stiffer film patterns with $\varepsilon_{Gap\text{-}x} = (L_{g0} - L_g)/L_{g0}$.

Figure 2(c) shows the Au wrinkling 3D profiles obtained by Atomic Force Microscopy (AFM Bruker™ 3100) scan with which they progressively grew under different substrate strains. Based on the critical wrinkling strain of $\varepsilon_w = 0.25(\frac{3\bar{E}s}{\bar{E}f})^{2/3}$, the expected theoretical $\varepsilon_w = 6.7 \times 10^{-4}$ calculated based on the elastic plane-strain moduli of $E_f = 7 \times 10^{10}$ Pa and 74 nm gold film of $E_s = 4 \times 10^5$ Pa. In reality, the wrinkles started to form at a substrate strain $\varepsilon_{sub} = 9 \times 10^{-3}$. This indicates and confirms that the local strains on stiff Au electrodes significantly lagged behind those of the substrate and soft PDMS gap areas, which is considered as a helpful technique to protect metal films under large compression strains. The wrinkles on Au continuously grew under further x-direction compression, covering the majority of the Au electrodes at the substrate strain of 0.12. The wrinkle wavelength at substrate strain $\varepsilon_{sub} = 0.12$ was calculated to be 17 μm according to $\lambda_0 = (2\pi h_f)(\frac{\bar{E}f}{3\bar{E}s})^{1/3}$, which closely agreed with

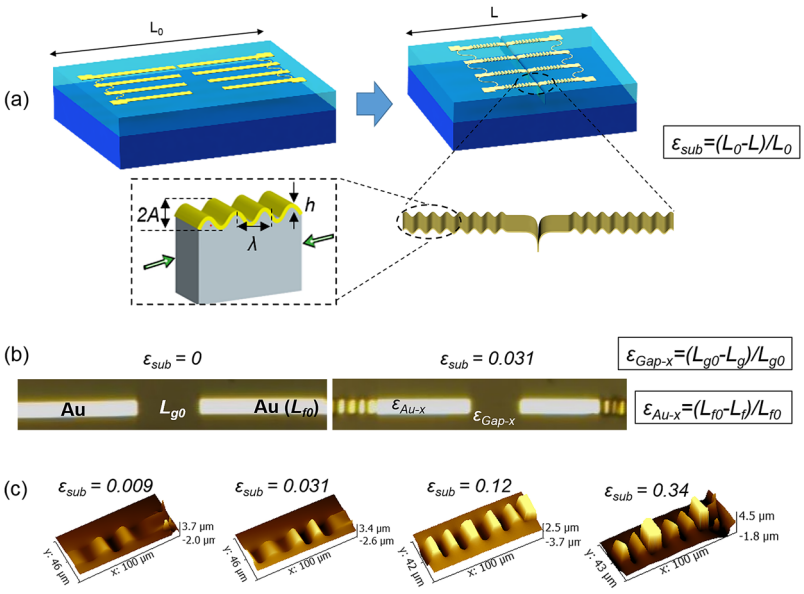

FIG. 2. (a) 3D Schematics showing the Au wrinkling—PDMS creasing 3D deformation process under uniaxial substrate compression—pair of finger electrodes into self-contact due to PDMS creasing, and wrinkling on Au finger electrodes. (b) Top view optical microscopic image showing local strain changes on Au due to wrinkling, and PDMS gap area due to creasing. (c) AFM scan 3D surface profile view of the wrinkle development on the Au electrode at various substrate strains for a device with W_f = 25 μm, L_g = 50 μm, and L_f = 225 μm.

the actual measured value of 18 μm (shown in the supplementary material).

To further understand this local strain difference between Au and PDMS areas against the substrate strain, characterization experiments were designed and conducted using a Nikon® LV-100 optical microscope. We focused on local strains of each Au finger electrodes $\varepsilon_{Au\text{-}x} = (L_{f0} - L_f)/L_{f0}$, as well as PDMS gap area $\varepsilon_{Gap\text{-}x} = (L_{g0} - L_g)/L_{g0}$ between the paired finger electrodes. The length data L_{f0}, L_f and L_{g0}, L_g were all measured by the Nikon system from top view. The relationships between $\varepsilon_{Au\text{-}x}$, $\varepsilon_{Gap\text{-}x}$, and ε_{sub} were comparatively studied against other key geometry design parameters of the Au electrodes such as L_f, L_g, finger width W_f, and locations in the transducer array (E, F1 to F4).

Figure 3(a) shows the relationship between the Au local strains against the substrate strains. The $\varepsilon_{Au\text{-}x}$ always lagged behind the ε_{sub} which is indicated by the dashed line. The strain gap was observed to be constantly ~0.03, until ε_{sub} = 0.45 where this gap increased to around 0.05 when large creases started to appear on PDMS surfaces which absorbed more strain energy. This has confirmed the previous assumption that the local strains on stiff Au electrodes significantly lagged behind those of the substrate. Together with the reversible wrinkling mechanism, most Au electrodes remain

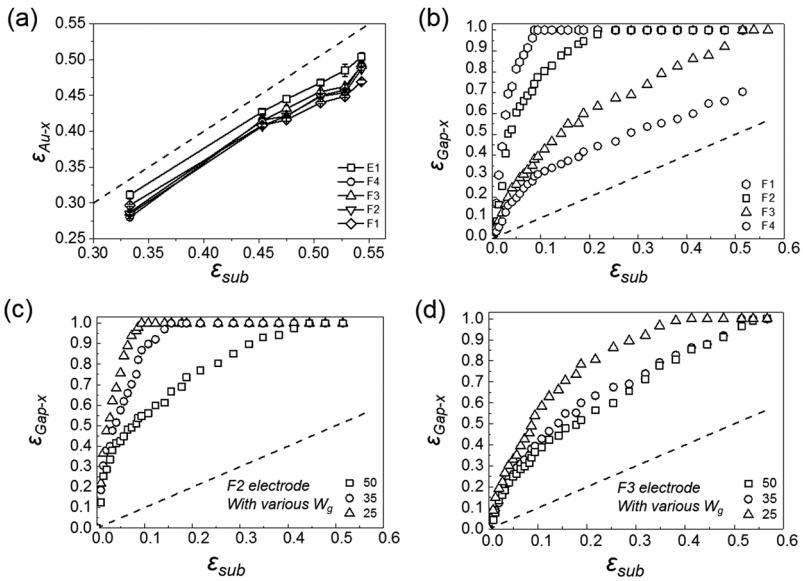

FIG. 3. Local strain change comparisons: (a) Au electrodes strain vs. substrate strain comparing F1 to F4, and contact pads E1. (b) The PDMS gap strain vs. substrate strain comparing between electrodes with varied L_{g0} and L_{f0}. [(c) and (d)] Finger electrode width W_f effect on the PDMS gap strain vs. substrate strain for F2 and F3 electrodes; all dashed lines indicate substrate strain value as a reference.

intact after >10 cycles of repeated compression. For determining the switching strain values that bring Au finger pair electrodes into self-contact, Figs. 3(b)–3(d) show detailed comparative results of the PDMS gap strain $\varepsilon_{Gap\text{-}x}$ versus the substrate strain ε_{sub}. When $\varepsilon_{Gap\text{-}x} = 1$ at $L_g = 0$, it was an indication that the PDMS area in the gap was completely folded into the crease from the top view, as illustrated in Fig. 2(a). The corresponding value of ε_{sub} at this point is close to the switching strain.

Figure 3(b) shows the comparison of results between different finger electrodes (F1 to F4) on the same transducer array where $W_f = 35\ \mu$m, initial L_{f0} ranges from 225 μm to 250 μm, and L_{g0} from 10 μm to 55 μm, respectively. All $\varepsilon_{Gap\text{-}x}$ are far greater than the ε_{sub} (indicated by a dashed line) due to the expected strain amplification effect. It can be observed that for a pair of electrodes F1 with smallest L_{g0}, the self-contact strain is around $\varepsilon_{sub} = 0.08$, which is significantly lower than typical creasing strains of around 50% on plain PDMS surfaces.[5,20] As L_g gradually increased, it required much higher substrate strains to bring F2 and F3 pair electrodes into self-contact, at $\varepsilon_{sub} = 0.2$ and $\varepsilon_{sub} = 0.5$, respectively. For F4 electrodes, it is understandable that the large L_{g0} made it impossible for the pair of electrodes to reach each other before the 0.6 substrate strain limit [Fig. 3(b)], due to insufficient self-contact depth (estimated to be around 19 μm) before reaching the limit. Since the natural wavelength of the crease is ~3.5 times of substrate thickness H ($H = 110\ \mu$m in this case), multiple creases may occur at larger distances, which prevents the electrodes from achieving contacts even at higher strains.

We also compared finger electrode width W_f (25 μm, 35 μm, and 50 μm) effect on gap strain $\varepsilon_{Gap\text{-}x}$, as shown in Figs. 3(c) and 3(d). The initial gap distance L_{g0} for F2 electrodes [Fig. 3(c)] was kept at 15 μm while L_{g0} for F3 [Fig. 3(d)] was kept at 25 μm. The electrode lengths L_{f0} are 250 μm and 245 μm, respectively. It was clearly observed in both cases that electrodes with narrow W_f (25 μm) had much lower ε_{sub} of 0.1 and 0.4, respectively, when the electrode pair made self-contact. This suggests that a wider Au electrode may require more energy to be pulled into the creasing created in the PDMS gap area, since the electrode prefers small wrinkling.

Based on the above deformation study, we demonstrated multi-step or "stepwise" electrical resistance change corresponding to different levels of ε_{sub}. The Everbeing EB8 manual probe station (with EB-05 probes) which connected to a Keithley® 4200 analyzer (I-V mode, −1 V to +1 V sweep, with 0.2 V/step) was used to characterize the resistance value change. As shown in Fig. 4, the step-wise strain-resistance sensing has been achieved by surface elastic instability induced multi-finger electrodes with different distances between the electrodes. For the designed L_g values ($L_f = 510\ \mu$m and 520 μm, respectively), the estimated finger electrode resistance would be in the region of 50 Ω. When the first pair of electrodes was in contact, the calculated resistance would be ~100 Ω, assuming that the contact resistance is zero. This will be reduced to 50 Ω when the second switching was achieved. Figure 4(b) shows greater details of the two-step switching resistance-strain relationship. Between 0.45 and 0.52, the first step switching stage was achieved, with a resistance of ~120 Ω. Under further compression, the second step switching stage occurred at the substrate strain range of $0.54 < \varepsilon_{sub} < 0.58$ by measuring the resistance to be ~50 Ω. Note that the error bars indicate multiple measurements at different current

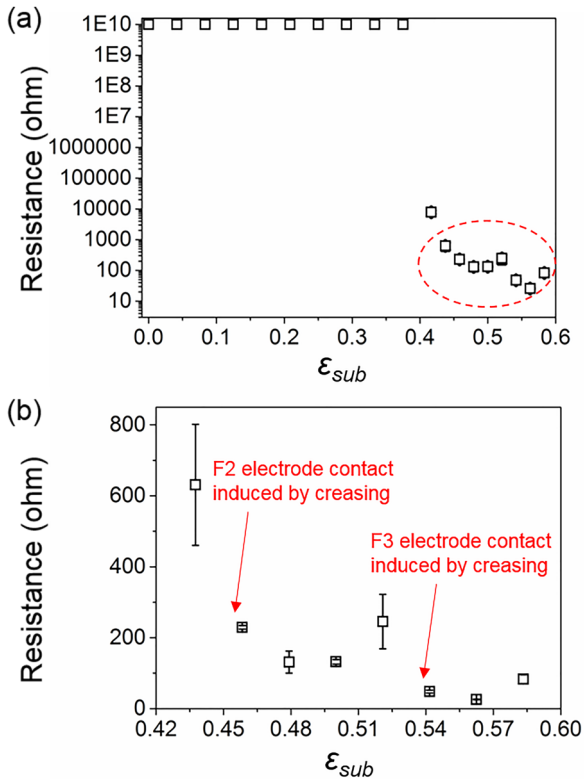

FIG. 4. (a) Resistance of the test structure as a function of strain. The resistance change during the two-stage switching is highlighted in a red ring and detailed in (b). Two-stage resistance switching strain sensing: Resistance of the transducer array as a function of strain during the two-stage switching period ($0.45 < \varepsilon < 0.52$ and $0.54 < \varepsilon < 0.6$) (b).

levels that in most cases indicate that Joule heating is not influencing the measurement. The probe-Au electrode contact resistance was characterized to be ~7.9 Ω with a standard deviation of 1.17. The variation of the experimental resistance values may be mainly caused by the contact resistance between the touching Au finger electrodes. The corresponding substrate strains at switching were also in good agreement with the electrode deformation observations.

In conclusion, a new strategy has been established to detect the multiple strain values on a soft elastic substrate to study the metal-elastomer deformation behavior of a super-compressible strain transducer array. We have characterized the relationship between electrode geometries and compression strain ratios, together with the growth and co-existence of wrinkles and creases on multi-switching electrodes. Multi-steps of electrical resistances were generated at different switching strains on an individual device. This has been demonstrated by using the multiple finger electrode soft electronics with different distances between the electrodes, which has potential for future stretchable/epidermal electronics, flexible sensors, health monitoring, and wearable device applications.

This supplementary material contains the experimental and fabrication method, as well as the additional results to support the results and claims in the main context.

This work was supported by EPSRC (Grant Nos. EP/N007921/1 and EP/L026899/1) and the Royal Society (Grant No. RG150662). The authors would like to thank Everbeing who donated the probing system used in this work, and MEMSstar, Ltd., for providing the SAM coating facility. Data associated with this paper are available via Northumbria Research Data Management scheme.

REFERENCES

[1] D.-H. Kim, N. Lu, R. Ma, Y.-S. Kim, R.-H. Kim, S. Wang, J. Wu, S. M. Won, H. Tao, A. Islam, K. J. Yu, T.-I. Kim, R. Chowdhury, M. Ying, L. Xu, M. Li, H.-J. Chung, H. Keum, M. McCormick, P. Liu, Y.-W. Zhang, F. G. Omenetto, Y. Huang, T. Coleman, and J. A. Rogers, Science **333**, 838–843 (2011).
[2] W. Wu, X. Wen, and Z. L. Wang, Science **340**, 952 (2013).
[3] W. Gao, S. Emaminejad, H. Y. Nyein, S. Challa, K. Chen, A. Peck, H. M. Fahad, H. Ota, H. Shiraki, D. Kiriya, D.-H. Lien, G. A. Brooks, R. W. Davis, and A. Javey, Nature **529**, 509 (2016).
[4] S. R. Madhvapathy, Y. Ma, M. Patel, S. Krishnan, C. Wei, Y. Li, S. Xu, X. Feng, Y. Huang, and J. A. Rogers, Adv. Funct. Mater. **28**, 1802083 (2018).
[5] B. Xu, D. Chen, and R. C. Hayward, Adv. Mater. **26**, 4381–4385 (2014).
[6] D.-Y. Khang, J. A. Rogers, and H. H. Lee, Adv. Funct. Mater. **18**, 1526–1536 (2008).
[7] T. Pan, M. Pharr, Y. Ma, R. Ning, Z. Yan, R. Xu, X. Feng, Y. Huang, and J. A. Rogers, Adv. Funct. Mater. **27**, 1702589 (2017).
[8] C. Wang, B. B. Xu, J. G. Terry, S. Smith, A. J. Walton, and Y. Li, in *Proceedings of the 30th International Conference on Microelectronic Test Structures, Grenoble, France* (IEEE, 2017), pp. 150–155.
[9] C. Wang, B. B. Xu, J. G. Terry, S. Smith, A. J. Walton, and Y. Li, in *1st IEEE International Flexible Electronics Technology Conference, Ottawa, Canada* (IEEE, 2018).
[10] Y. Chu, X. Wu, J. Lu, D. Liu, J. Du, G. Zhang, and J. Huang, Adv. Sci. **3**, 1500435 (2016).
[11] D. Chen, L. Jin, Z. Suo, and R. C. Hayward, Mater. Horiz. **1**, 207 (2014).
[12] C. Wang, C. Wang, Z. Huang, and S. Xu, Adv. Mater. **30**, 1801368 (2018).
[13] X. Xue, S. Wang, C. Zeng, L. Li, and C. Li, Surf. Interface Anal. **50**, 180–187 (2018).
[14] K. E. Crawford, Y. Ma, S. Krishnan, C. Wei, D. Capua, Y. Xue, S. Xu, Z. Xie, S. M. Won, L. Tian, C. Webb, Y. Li, X. Feng, Y. Huang, and J. A. Rogers, Extreme Mech. Lett. **22**, 27–35 (2018).
[15] Y.-C. Chen and A. J. Crosby, Adv. Mater. **26**, 5626–5631 (2014).
[16] C. F. Guo, Q. Liu, G. Wang, Y. Wang, Z. Shi, Z. Suo, C.-W. Chu, and Z. Ren, Proc. Natl. Acad. Sci. U. S. A. **112**, 12332 (2015).
[17] X. Guo, X. Wang, D. Ou, J. Ye, W. Pang, Y. Hung, J. A. Rogers, and Y. Zhang, npj Flexible Electron. **14**, 14 (2018).
[18] A. Auguste, L. Jin, Z. Suo, and R. C. Hayward, Extreme Mech. Lett. **11**, 30–36 (2017).
[19] D. Wang, N. Cheewaruangroj, Y. Li, G. Mchale, Y. Jiang, D. Wood, J. S. Biggins, and B. B. Xu, Adv. Funct. Mater. **28**, 1704228 (2018).
[20] D. Chen, S. Cai, Z. Suo, and R. C. Hayward, Phys. Rev. Lett. **109**, 038001 (2012).
[21] T. Ouchi, J. Yang, Z. Suo, and R. C. Hayward, ACS Appl. Mater. Interfaces **10**, 23406–23413 (2018).
[22] K. Nan, H. Luan, Z. Yan, X. Ning, Y. Wang, A. Wang, J. Wang, M. Han, M. Chang, K. Li, Y. Zhang, W. Huang, Y. Xue, Y. Huang, Y. Zhang, and J. A. Rogers, Adv. Funct. Mater. **27**, 1604281 (2017).
[23] G. Lee, T. Lee, Y. W. Choi, P. V. Pikhitsa, S. J. Park, S. M. Kim, D. Kang, and M. Choi, J. Mater. Chem. C **5**, 10920 (2017).
[24] D. Rhee, W.-K. Lee, and T. Odom, Angew. Chem., Int. Ed. **56**, 6523 (2017).
[25] H. Lu, Y. Liu, B. Xu, D. Hui, and Y. Fu, Composites, Part B **122**, 9 (2017).
[26] B. Xu and R. Hayward, Adv. Mater. **25**, 5555 (2013).
[27] J. Kim, J. Yoon, and R. Hayward, Nat. Mater. **9**, 159 (2010).
[28] S. Cai, D. Chen, Z. Suo, and R. Hayward, Soft Matter **8**, 1301 (2012).
[29] B. Xu, Q. Liu, Z. Suo, and R. Hayward, Adv. Funct. Mater. **26**, 3218 (2016).